Published in final edited form as:
J Am Chem Soc. 2009 April 8; 131(13): 4685–4694. doi:10.1021/ja808346y.

Transition States of *Plasmodium falciparum* and Human Orotate Phosphoribosyltransferases†

Yong Zhang#, **Minkui Luo**, and **Vern L. Schramm***
Contribution from the Department of Biochemistry, Albert Einstein College of Medicine, Bronx, New York 10461.

Abstract

Orotate phosphoribosyltransferases (OPRT) catalyze the formation of orotidine 5′-monophosphate (OMP) from α-D-phosphoribosylpyrophosphate (PRPP) and orotate, an essential step in the *de novo* biosynthesis of pyrimidines. Pyrimidine *de novo* biosynthesis is required in *Plasmodium falciparum*, thus OPRT of the parasite (*Pf*OPRT) is a target for anti-malarial drugs. *De novo* biosynthesis of pyrimidines is also a feature of rapidly-proliferating cancer cells. Human OPRT (*Hs*OPRT) is therefore a target for neoplastic and autoimmune diseases. One approach to the inhibition of OPRTs is through analogues that mimic the transition states of *Pf*OPRT and *Hs*OPRT. The transition state structures of these OPRTs were analyzed by kinetic isotope effects (KIEs), substrate specificity and computational chemistry. With phosphonoacetic acid (PA), an analogue of pyrophosphate, the intrinsic KIEs of [1′-^{14}C], [1, 3-$^{15}N_2$], [3-^{15}N], [1′-^{3}H], [2′-^{3}H], [4′-^{3}H] and [5′-$^{3}H_2$] are 1.034, 1.028, 0.997, 1.261, 1.116, 0.974 and 1.013 for *Pf*OPRT and 1.035, 1.025, 0.993, 1.199, 1.129, 0.962 and 1.019 for *Hs*OPRT, respectively. Transition state structures of *Pf*OPRT and *Hs*OPRT were determined computationally by matching the calculated and intrinsic KIEs. The enzymes form late associative $D_N{*}A_N^{\ddagger}$ transition states with complete orotate loss and partially-associative nucleophile. The C1′-O^{PA} distances are approximately 2.1 Å at these transition states. The modest [1′-^{14}C] KIEs and large [1′-^{3}H] KIEs are characteristic of $D_N{*}A_N^{\ddagger}$ transition states. The large [2′-^{3}H] KIEs indicate a ribosyl 2′-C-*endo* conformation at the transition states. *p*-Nitrophenyl β-Dribose 5′-phosphate is a poor substrate of *Pf*OPRT and *Hs*OPRT but is a nanomolar inhibitor, supporting a reaction coordinate with strong leaving group activation.

Introduction

Plasmodium falciparum is a protozoan parasite that causes a severe form of human malaria. It is estimated that over one million people die annually of *P. falciparum*-related malaria with a majority under the age of five.[1] The development of new therapeutic approaches against malaria is urgent due to the increased resistance to current anti-malarial drugs.[2,3] For *P. falciparum* and humans, *de novo* pyrimidine biosynthesis is the major pathway of nucleotide production. The viability of *P. falciparum* depends completely upon *de novo* pyrimidine biosynthesis, but mammals can also use a salvage pathway.[4] *P. falciparum* does not encode enzymes of the pyrimidine salvage pathway.[4-7] Inhibitors against *de novo* pyrimidine biosynthesis are fatal for the parasite.[8-10]

†Supported by research grant AI049512 from the National Institute of Health

#Present address: Memorial Sloan-Kettering Cancer Center, 1275 York Avenue, New York, NY 10065.
*E-mail: vern@aecom.yu.edu

Supporting Information Available: Full author list of Ref.48 and complete calculation results. This material is available free of charge via the Internet at http://pubs.acs.org.

De novo pyrimidine biosynthesis requires six sequential reactions to generate uridine 5′-monophosphate (UMP).[4,11] Orotate phosphoribosyltransferase (EC 2.4.2.10, OPRT) is the fifth enzyme and catalyzes the formation of orotidine 5′-monophosphate (OMP) from α-D-phosphoribosylpyrophosphate (PRPP) and orotate. OMP is subsequently converted to UMP by OMP decarboxylase (ODC). Given the essential function of UMP biosynthesis in *P. falciparum*, blocking OMP production may provide anti-malarial compounds.

OPRT homologues are widely distributed among bacteria, fungi, insect and mammals.[12] OPRT and ODC activities of most prokaryotes are located in two separately encoded enzymes. However, in higher eukaryotes both activities are associated within a single bifunctional protein, UMP synthase.[4,13-19] Human UMP synthase (*Hs*UMPase) contains N-terminal OPRT and C-terminal ODC domains.[20] It plays an essential role in the rapidly-proliferating cells, because these cells rely on *de novo* pyrimidine biosynthesis to satisfy the increased demand for nucleic acid synthesis.[21] This feature has been successfully exploited in other inhibitors of *de novo* pyrimidine biosynthesis, including the antifolates. Anti-pyrimidine therapies are in use for the treatment of malignant neoplastic and autoimmune diseases.[22-26] The human OPRT (*Hs*OPRT) domain of *Hs*UMPase provides another potential target for anti-cancer and immunosuppressive drugs.

Transition state theory predicts that transition state analogues bind more tightly to enzymes than substrates by the factor of catalytic rate acceleration. With typical accelerations of 10^{10}-10^{15} and substrate affinity of 10^{-3}-10^{-6} M, enzymes are expected to bind faithful mimics of transition state analogues with K_d values in the range of 10^{-14}-10^{-23} M.[27-33] Transition state analogues can be designed from transition state models based on kinetic isotope effects (KIEs) interpreted through computational chemistry to match experimental and computed KIE values. Consequently, KIEs provide a powerful tool to access enzymatic transition state structures.[30,32,34]

The intrinsic KIEs of *Pf*OPRT and *Hs*OPRT at geometry-sensitive positions were measured with phosphonoacetic acid (PA) as a slow substrate analogue of pyrophosphate and used as constraints for computational chemistry to explore their transition state structures (Figure 1). The transition states are characterized by ribooxacarbenium ion character and fully dissociated orotate. Significant nucleophilic attack is involved at the OPRT transition states ($D_N{*}A_N^{\ddagger}$). For enzymes with ribocations at their transition states, nitrophenylribosides provide mechanistic tools for distinguishing leaving group from ribocation activation.[35] *p*-Nitrophenyl β-D-ribose 5′-phosphate was synthesized with deoxyribonucleoside kinase (Figure 2).[36] Poor catalytic activity with OPRTs indicate that leaving group activation is important for *Pf*OPRT and *Hs*OPRT. The $D_N{*}A_N^{\ddagger}$ transition states of *Pf*OPRT and *Hs*OPRT are different from the partially dissociative $D_N^{\ddagger}{*}A_N$ transition state of *Salmonella typhimurium* OPRT (*St*OPRT).[37] The OPRT transition states provide blueprints for the design of transition state analogues.

Experimental Methods

Protein Expression Vector

The genes for *Pf*OPRT and *Hs*UMPase with a thrombin-cleavable His_6 tag at the N-terminal were synthesized chemically and cloned into the pDONR221 vector (DNA 2.0, Menlo Park, CA). Gene codons were optimized by adopting the commonly used codons (>10% usage frequency) in *E.coli*. The *Pf*OPRT and *Hs*UMPase genes were then recombined with the pDEST14 vector via LR Clonase II reaction (Invitrogen). The subsequent pDEST14-*Pf*OPRT vector was used for protein expression. For the pDEST14-*Hs*UMPase vector, a stop codon was introduced at L246 with QuikChange® II XL Site-Directed Mutagenesis Kits (La Jolla, CA). This *Hs*UMPase truncation construct only expresses its *Hs*OPRT domain. The plasmid genes were sequenced to confirm the integrity.

Expression and Purification of *Pf*OPRT and *Hs*OPRT

The pDEST14 vectors encoding the two OPRT genes were transformed into BL21-AI *E. coli* competent cells and grown in LB + Amp (100 μg mL^{-1}) at 37 °C to an OD_{600} of 0.6. Protein expression was induced by adding 0.02% L-arabinose with overnight growth at 37 °C. Cells were harvested by centrifugation at 4 °C, weighted and resuspended in lysis buffer (20 mM Tris-HCl, 500 mM NaCl and 5 mM Imidazole, pH = 7.9, 3 mL/gram cell pellet). Lysozyme (100 μg mL^{-1}), DNase I (10 μg mL^{-1}) and protease inhibitor (1 tablet/8 grams of cells)(Roche Applied Science, Indianapolis, IN) were added to the solution. Following disruption in a French Press, cell lysate was centrifuged at 30,000 g for 25 min at 4 °C. The supernatant was loaded onto a Ni^{2+} affinity column, washed with 5 column volume of binding buffer (the same as lysis buffer) and washed with 20 mM Tris-HCl, 500 mM NaCl and 20 mM Imidazole, pH = 7.9. The 6×His-OPRTs were eluted with a gradient of imidazole (20 mM ~ 500 mM). The OPRT bands were visualized on SDS-PAGE gels and fractions with high purity were pooled, made to 10% glycerol and 10 mM β-ME (final concentration), concentrated and dialyzed overnight at 4 °C to remove imidazole. His-tags were removed during dialysis by the presence of thrombin (1 unit/0.1 mg). His-tag free OPRTs were purified by Superdex 200 26/60 Gel filtration column, concentrated and stored at −80 °C. The enzyme activities were tested at 25 °C in mixtures containing 50 mM Tris-HCl, 5 mM $MgCl_2$, pH = 8.0 and varied concentrations of OMP and pyrophosphate. Reactions were monitored by the absorbance increase at 295 nm to give an extinction coefficient of 3.67 mM^{-1} cm^{-1}.

Reagents and Materials

D-[6-$^3H_2$]glucose-6-phosphate, D-[5-^{3}H]glucose, D-[6-^{14}C]glucose, D-[1-^{3}H]ribose and D-[1-^{14}C]ribose were purchased from American Radiolabeled Chemicals Inc.. [1, 3-$^{15}N_2$]orotic acid and [$^{15}N_2$]urea were purchased from Cambridge Isotope Laboratories. *p*-Nitrophenyl β-D-ribose was generously provided by Dr. Peter C. Tyler (Industrial Research Ltd., New Zealand). [2-^{3}H]ribose was synthesized as described previously.[38-40] Hexokinase (HK), glucose-6-phosphate dehydrogenase (G6PDH), phosphogluconic acid dehydrogenase (PGDH), L-glutamic acid dehydrogenase (GDH), phosphoriboisomerase (PRI), adenylate kinase (AK) and pyruvate kinase (PK) were purchased from Sigma. Phospho-D-ribosyl-α-1-pyrophosphate synthase (PRPPase) and ribokinase (RK) were prepared as described before.[41,42] Deoxynucleoside kinase from *Anopheles gambiae* (Ag-dNK) was kindly provided by Dr. Maria B. Cassera (Department of Biochemistry, Albert Einstein College of Medicine). All other reagents were purchased from readily available commercial sources and used without further purification. Nitrogen nuclear magnetic resonance (^{15}N NMR) was measured in DMSO-d_6 using a Bruker 300 MHz instrument. The ^{15}N NMR spectra were collected using continuous proton-decoupling mode with at least 10000 scans. Mass spectra were acquired on an IonSpec FT-ICR mass spectrometer (Varian Inc., CA).

Synthesis of [3-^{15}N]orotic acid

[3-^{15}N]Orotic acid was synthesized based on previous reports with some modifications.[43, 44] Briefly, 1.47 g of DL-aspartic acid, 1.74 g of KOH and 0.66 g of [$^{15}N_2$]urea were dissolved in 33.3 mL of water. The mixture was refluxed at 115 °C for 2 hr, then two portions of 0.66 g of [$^{15}N_2$]urea were added separately with a 2 hr interval. After 6 hr reaction, the mixture was acidified with 3 mL of concentrated HCl and allowed to stand overnight at room temperature. Precipitated ureidosuccinic acid was filtrated and recrystallized from water. Ureidosuccinic acid (0.82 g) was dissolved in 2.73 mL of 20% HCl. The mixture was evaporated to dryness on a hot plate. The resulting 5-acetic acid-hydantoin was recrystallized from water. Crystals (0.62 g) were mixed with 2.46 mL of glacial acetic acid and 0.62 g of bromine and heated at 100 °C in a sealed tube for 2 hr. Precipitated 5-carboxymethylidine-hydantoin was filtrated, recrystallized from water and 0.42 g of the product was added to 14 mL of 1 M KOH. Following

64 °C for 2 hr, the [3-^{15}N]orotic acid was precipitated by acidification with concentrated HCl and recrystallization from water. [3-^{15}N]orotic acid: ^{15}N NMR (75 MHz, DMSO-d_6) δ 15 ppm 161; *m/z* std $C_5H_5N_2O_4$ (M+1) 157.026, $C_5H_5{}^{15}N_1N_1O_4$ (M+1) 158.023.

Synthesis of Isotopically Labeled OMPs

[1′-^{3}H]OMP, [1′-^{14}C]OMP and [2′-^{3}H]OMP were prepared enzymatically from [1-^{3}H]ribose, [1-^{14}C]ribose and [2-^{3}H]ribose, respectively. [4′-^{3}H]OMP, [5′-$^{3}H_2$]OMP and [5′-^{14}C]OMP were synthesized from [5-^{3}H]glucose, [6-$^{3}H_2$]glucose-6-phosphate and [6-^{14}C]glucose, respectively. [3-^{15}N]OMP and [1, 3-$^{15}N_2$]OMP were synthesized with [3-^{15}N]- and [1, 3-$^{15}N_2$]orotic acid as precursors, respectively (eg. Figure 3).

Synthesis of OMP from ribose and orotate used a reaction mixture with 2.5 mM orotate, 1 mM ribose, 100 mM phosphate (pH = 7.4), 50 mM glycylglycine, 50 mM KCl, 20 mM $MgCl_2$, 20 mM phosphoenolpyruvate, 1 mM ATP and 2 mM DTT. The reactions were initialized by adding an enzyme mixture containing 1 unit AK, 1 unit PK, 0.01 unit RK, 0.008 unit PRPPase and 0.033 unit *Pf*OPRT. This reaction mixture was incubated at 37 °C for 20 hr to reach completion. OMP products were then purified twice by reverse phase HPLC (C-18 Deltapak column, 20 mM KH_2PO_4, 8 mM tetrabutylammonium, pH = 6.0 as eluting buffer). The OMPs were concentrated and repurified by HPLC, eluted with 2% (v/v) MeOH/H_2O. The overall yields of OMP varied from 40% and 90% with reference to ribose.

For OMP synthesis from glucose, the reactions contained 2.5 mM orotate, 1 mM glucose, 100 mM phosphate, 50 mM glycylglycine, 50 mM KCl, 20 mM $MgCl_2$, 5 mM NH_4Cl, 20 mM phosphoenolpyruvate, 1 mM ATP, 0.1 mM $NADP^+$, 20 mM α-keto glutarate and 2 mM DTT (pH = 7.4). The reaction was initialized by adding 1 unit HK, 1 unit G6PDH, 0.075 unit PGDH, 0.02 unit PRI, 1 unit GDH, 0.016 unit PRPPase, 0.033 unit *Pf*OPRT, 1 unit AK and 1 unit PK (pre-mixed enzyme solution). The reaction mixture was then incubated at 37 °C for 20 hr to generate OMP. The OMP products were purified as described above. The overall yields of OMP were 30% to 70% from starting glucose. After the last step of HPLC purification (described above), isotopically labeled OMPs were lyophilized, dissolved in H_2O and stored in −80 °C for further use.

Determination of Kinetic Isotope Effects

KIEs were measured under competitive conditions using the isotope ratio method. Briefly, the ^{3}H- and ^{14}C-labeled OMPs were mixed at a ratio of 4:1 (cpm) with at least 5×10^4 cpm for ^{14}C. The OMP mixture was then added into a solution containing 50 mM Tris-HCl (pH = 8.0), 5 mM $MgCl_2$, 20 mM PA and 100 μM OMP (labeled and unlabeled). All the experiments were performed at 25 °C with 1.2 mL reaction volume in the presence of either 0.7 μM *Pf*OPRT or 0.9 μM *Hs*OPRT. Part of the reaction mixture (240 μL) was allowed to proceed to 100% completion by adding another 4.5 μM *Pf*OPRT (final concentration) and incubating an additional 4 hr. The rest of the reaction was stopped at 20 to 30% conversion to product. The two reaction mixtures (100% and 20-30%) were loaded onto charcoal-cellulose column (1:4 w/w, pre-equilibrated with H_2O), followed by washing with 1 mL H_2O. The isotopically labeled reaction products were then eluted with 3 mL 3.3% (v/v) NH_4OH/H_2O (to pH = 6.6 with acetic acid). The 3 mL fractions were dried by speedvac, mixed with 200 μL H_2O and then 10 mL scintillation counter cocktail (Ultima Gold) as described before.[39,40] These samples were counted for at least 8 cycles to give ^{3}H:^{14}C ratios (20 min/cycle, Wallac 1414 LSC, PerkinElmer) and averaged. For each KIE measurement at least 5 replicates were performed.

The ^{14}C channel ratio was calculated by determining the ratio between channel 1 and channel 2 through counting the [1-^{14}C]ribose standard. The channel 1 and 2 were set to keep all ^{3}H

signals in channel 1, whereas only ^{14}C counts appear in channel 2. The following equations were used for data processing:

$$\text{cpm}\ \left(^{3}\text{H}\right)=\text{cpm}_{\text{channel 1}}-\text{cpm}_{\text{channel 2}}\times\left(^{14}\text{C channel ratio}\right)$$

$$\text{cpm}\ \left(^{14}\text{C}\right)=\text{cpm}_{\text{channel 2}}\times\left(1+^{14}\text{C channel ratio}\right)$$

The ^{3}H:^{14}C ratio was determined for the partial and complete conversion. The KIEs were corrected to 0% reaction based on the eq. 1, where *f* is the fraction of the reaction completion, R_f and R_0 are the ratios of the heavy isotope to the light isotope at the partial and complete conversion, respectively.

$$KIE=\frac{\ln\left(1-f\right)}{\ln\left(1-f\times\frac{R_f}{R_0}\right)} \quad (1)$$

Measurement of Forward Commitment Factor

The forward commitment factors of OPRT-catalyzed reactions were measured by isotope trapping enzyme-bound radiolabeled substrate in the presence of excessive unlabeled substrate.[39,40,45-47] Briefly, 31 μM OPRT was pre-incubated with 60 μM [1, 3-$^{15}N_2$, 5′-^{14}C]OMP for 10 s at 25 °C in a total volume of 10 μL solution (50 mM Tris-HCl, 5 mM $MgCl_2$ and pH = 8.0). The reaction mixture was rapidly chased with 140 μL buffer containing 50 mM Tris-HCL (pH = 8.0), 5 mM $MgCl_2$, 5 mM unlabeled OMP and various concentrations of PA. After five catalytic turnovers, the reaction mixture was loaded onto the charcoal:cellulose column (1:4, w/w) pre-equilibrated with H_2O, followed by washing with 1 mL H_2O. Products were eluted with 3 mL 3.3% (v/v) NH_4OH/H_2O (pH = 6.6) and the radioactivity of products were determined by liquid scintillation counting. Control experiments in the absence of enzyme provided background correction. The specific radioactivity of labeled product vs bound substrate in the Michaelis complex was plotted against PA concentrations (Figure 4). The forward commitment factors were calculated on the basis of the equation $C_f=\frac{Y_{max}}{1-Y_{max}}$, where Y_{max} is the y axial intercept upon extrapolating the max plateau region and C_f is forward commitment factor.

Computational Modeling of Transition State Structures

The transition state structures were determined *in vacuo* by hybrid density functional theory implemented in Gaussian 98.[48] The structures of OMP and 5′-phosphoribosyl oxacarbenium ion containing partly or fully dissociated orotate in different ionization states and with varied extents of PA nucleophilic participation were optimized using B3LYP functional and 6-31G (d, p) basis sets. To match the intrinsic KIEs obtained experimentally, the bond distances of C1′-N1 and C1′-O^{PA} were varied systematically. The bond frequencies of substrate and transition states were calculated at the same level of theory and basis sets. Computational KIEs were obtained on the basis of bond frequency changes from substrate to transition states at the temperature of 298 K using the ISOEFF98 program.[49] All 3*N*-6 vibrational modes were used for calculation. The bond frequencies of substrate, transition state and a reaction-coordinate imaginary frequency of 50i cm^{-1} (or greater) were retrieved as input files to calculate the isotope effects. The transition state structures were iteratively altered and optimized until the calculated KIEs provided a best match to the intrinsic KIEs.

Calculation of Molecular Electrostatic Potential Surfaces

The molecular electrostatic potential (MEP) surfaces were calculated by employing the CUBE program in Gaussian 98. The checkpoint files for CUBE inputs were generated during geometry optimization at the B3LYP/6-31G (d, p) level. The MEP surfaces were visualized by Molekel 4.0 at a density of 0.2 electron/Å^3.[50,51]

Synthesis of *p*-nitrophenyl β-D-ribose 5′-phosphate and enzymatic activity assay

p-Nitrophenyl β-D-ribose 5′-phosphate was synthesized by 5′-phosphorylation of *p*-nitrophenyl β-D-ribose by Ag-dNK. The reaction mixtures contained 50 mM Tris-HCl (pH = 8.0), 5 mM $MgCl_2$, 50 mM KCl, 0.2 mM DTT, 8 mM ATP, 4 mM *p*-nitrophenyl β-D-ribose and 7 μM Ag-dNK. After overnight incubation at 37 °C, *p*-nitrophenyl β-D-ribose 5′-phosphate was purified by reverse phase HPLC (C-18 Deltapak column) with a gradient of acetonitrile from 3% to 30% in a buffer containing 100 mM KH_2PO_4 (pH = 6.0) and 8 mM tetrabutylammonium. *p*-Nitrophenyl β-D-ribose 5′-phosphate was then concentrated by rotovap, repurified by HPLC using elution with methanol from 2% to 50% in H_2O to provide a 28% overall yield, concentrated and stored at −80 °C. The *p*-nitrophenyl β-D-ribose 5′-phosphate: *m/z* $C_{11}H_{13}NO_{10}P$ (M-1) 350.029 observed; 350.028 calculated.

The *Pf*OPRT and *Hs*OPRT catalytic activities with *p*-nitrophenyl β-D-ribose 5′-phosphate were measured at 25 °C in solutions containing 50 mM Tris-HCl (pH = 8.0), 5 mM $MgCl_2$ and varied concentrations of *p*-nitrophenyl β-D-ribose 5′-phosphate and PA or pyrophosphate. Reaction rates were monitored through the absorbance increase at 400 nm.

Results and Discussion

Experimental KIEs, Commitment factor and Intrinsic KIEs

The experimental KIEs were measured under competitive conditions. The 5′-^{14}C of OMP is four bonds away from the reaction center and the [5′-^{14}C] KIE is assumed to be unity. The observed KIEs of [1′-^{3}H], [2′-^{3}H], [4′-^{3}H] and [5′-$^3H_2$] were determined with [5′-^{14}C]OMP as the silent remote label. The KIEs of [1′-^{14}C], [1, 3-$^{15}N_2$, 5′-^{14}C], [3-^{15}N, 5′-^{14}C] and [1, 3-$^{15}N_2$, 1′-^{14}C] were obtained with reference to [4′-^{3}H]OMP as the remote label. These observed KIEs were then corrected for the corresponding KIE of the remote label ([4′-^{3}H]) to give experimental KIEs.

The experimental KIEs contained the contribution from the commitment to the catalysis (commitment factors), which can mask intrinsic KIEs under some circumstances.[39,40] However, the commitment factors (forward and reverse) on intrinsic KIEs are within experimental error limits for *Pf*OPRT and *Hs*OPRT with PA as a slow substrate. The forward commitment factors of 0.035 for *Pf*OPRT and 0.042 for *Hs*OPRT were applied in the equation $^x(V/K) = (^xk + C_f)/(1 + C_f)$.[52] Here $^x(V/K)$ is the experimental KIE, ^xk is the intrinsic KIE and C_f is the forward commitment factor. The experimental $^x(V/K)$ and the intrinsic KIE (^xk) were the same within experimental error (Figure 4 and Table 1). This result is expected for PA as slow substrate with a small k_{cat} of 0.023 s^{-1} for *Pf*OPRT and 0.017 s^{-1} for *Hs*OPRT, and a large K_m of 1.59 mM for *Pf*OPRT and 3.84 mM for *Hs*OPRT. In cases where k_{cat}/K_m is small, forward commitment is minimized.[39,40,45] *Pf*OPRT and *Hs*OPRT display large [1′-^{3}H] $^T(V/K)$ KIEs and are near the theoretical maxima for [1, 3-$^{15}N_2$] $^N(V/K)$ KIEs. These values support a dissociated orotate (Table 1 and discussion below). Large KIE values also indicate that the reverse commitments of *Pf*OPRT and *Hs*OPRT have negligible effects on intrinsic KIE values.[41,53-55] Significant reverse commitment causes experimental KIE $^x(V/K)$ to be smaller than intrinsic ^xk. Experimental KIEs shown in Table 1 are therefore intrinsic KIEs for *Pf*OPRT and *Hs*OPRT.

When PPi was used to determine the KIEs, it was found that the [1′-^{14}C] and [1′-^{3}H] KIEs were 1.006 and 1.009 for *Pf*OPRT, and 1.007 and 1.008 for *Hs*OPRT, respectively. Due to high forward and/or internal commitment to catalysis, the primary [1′-^{14}C] and secondary [1′-^{3}H] KIEs were diminished with PPi. Intrinsic KIEs were readily obtained with PA as a slow substrate. An unknown in the use of alternate substrates for KIE analysis is if PA forms an altered transition state for *Pf*OPRT and *Hs*OPRT. In other cases, transition state analysis with substrate analogues has proven useful for the design of transition state analogues, one of the goals of the research program on OPRT.

Modeling Transition States

Transition state structures were estimated by computational modeling with experimental intrinsic KIEs as constraints. All calculations were carried out *in vacuo* at the B3LYP/6-31G (d, p) level. The geometry of the substrate OMP was first optimized without constraints and this geometry was maintained for transition state analysis. Large [1′-^{3}H] KIEs around 20% combined with modest [1′-^{14}C] KIEs of 3.5% are indicative of ribocationic transition state features with weak bonding to C1′(Figure 5). Consequently, the transition state optimization started with a 5′-phosphoribosyl oxacarbenium ion containing weak bonding to orotate or to PA. Bond distances between 1.8 Å to 2.6 Å were searched for C1′-N1 and C1′-O^{PA} to match intrinsic [1′-^{14}C] KIE and [1, 3-$^{15}N_2$]KIE for *Pf*OPRT and *Hs*OPRT. Only transition state structures with the C1′-N1 distances ≥ 2.6 Å agreed with the [1, 3-$^{15}N_2$]KIEs. The C1′-O^{PA} bond distances in the range of 2.14 ~ 2.15 Å are consistent with [1′-^{14}C], [1′-^{3}H] and [2′-^{3}H] KIEs (Table 1).

Geometries at the 4′- and 5′- regions of the transition states were optimized to match [4′-^{3}H] and [5′-^{3}H] intrinsic KIEs. OPRT crystal structures with OMP suggest geometry for the OMP 5′- regions.[56,57] These 5′-conformations were optimized using constraints to match experimental [4′-^{3}H] and [5′-$^{3}H_2$] KIEs.

Transition State Structures of *Pf*OPRT and *Hs*OPRT

Alignment between *Pf*OPRT and *Hs*OPRT indicated that they share only 26% identity in amino acid sequence. However, the intrinsic KIEs indicate that their transition states are similar in regard to orotate dissociation, the nature of their oxacarbenium ions at the transition state, nucleophilic participation and ribosyl conformation. The intrinsic KIEs for [1′-^{3}H], [2′-^{3}H], [4′-^{3}H], [5′-$^{3}H_2$], [1′-^{14}C], [1, 3-$^{15}N_2$, 5′-^{14}C], [3-^{15}N, 5′-^{14}C] and [1, 3-$^{15}N_2$, 1′-^{14}C] serve as boundary conditions to define the transition state structures of *Pf*OPRT and *Hs*OPRT (Table 1). The *Pf*OPRT and *Hs*OPRT transition state structures both display late associative D_N*$A_N^{‡}$ characteristics. This transition state is developed after formation of a ribooxacarbenium species with fully dissociated orotate and partial bonding to the attacking PA. The orotates at these transition states are at least 2.6 Å distant from the anomeric carbons (Figure 6). The characteristic ribooxacarbenium ions show a C1′-O^{PA} distance of 2.15 Å for *Pf*OPRT and 2.14 Å for *Hs*OPRT transition states. These distances are derived from the primary [1′-^{14}C] and [1, 3-$^{15}N_2$] intrinsic KIEs by matching calculated KIEs (Table 1). In the *Pf*OPRT and *Hs*OPRT transition state structures, the ribosyl rings both adopt 2′-C-*endo* conformations, giving a calculated [2′-^{3}H] KIEs of 14%, consistent with the observed KIEs of 12 to 13%. The 5′-regions of the transition states with a C3′-C4′-C5′-O5′ dihedral angle of −147° are consistent with the [4′-^{3}H] and [5′-$^{3}H_2$] KIEs.

The late D_N*$A_N^{‡}$ transition states of *Pf*OPRT and *Hs*OPRT are distinct from other *N*-ribosyltransferase enzymes. Most purine *N*-ribosyltransferase transition state structures have neutral leaving groups resulting from N7 protonation. In the *Pf*OPRT and *Hs*OPRT transition states, the leaving group orotates appear anionic as indicated by the leaving group ^{15}N KIE values discussed below.

[1, 3-$^{15}N_2$] and [3-^{15}N] KIEs

The [1, 3-$^{15}N_2$] and [3-^{15}N] KIEs of *Pf*OPRT and *Hs*OPRT arise from the extent of C1′-N1 bond dissociation as well as leaving group interactions of orotate at the transition states. Without protonation at the transition states, the calculated [1-^{15}N] KIE for a fully dissociated orotate dianion is 1.021, near the theoretical maximum. The [3-^{15}N] contributes an additional KIE of 1.004 to give the theoretical [1, 3-$^{15}N_2$] KIE of 1.025, consistent with the experimental [1, 3-$^{15}N_2$] KIEs of 1.028 for *Pf*OPRT and 1.025 for *Hs*OPRT. The calculated [3-^{15}N] KIE of 1.004 for dissociated orotate agrees with the intrinsic [3-^{15}N] KIEs of 0.997 for *Pf*OPRT and 0.993 for *Hs*OPRT. Transition state modeling indicated that protonation at O2, O4 or O7 (the exocyclic carboxyl group) causes the expected [1, 3-$^{15}N_2$] and [3-^{15}N] KIEs to be inconsistent with experimental values (Table 2). On the basis of the intrinsic [1, 3-$^{15}N_2$] and [3-^{15}N] KIEs, the *Pf*OPRT and *Hs*OPRT transition states display full loss of the C1′-N1 bond order to generate dianionic orotates. Despite the apparent lack of protonation of the leaving group, the anionic charge is likely to be stabilized by multiple hydrogen bond or ion-pair interactions at the catalytic site. Isotope effects are most sensitive to atomic bond changes and these electrostatic interactions are not likely to be represented in the KIEs.

Full loss of the C1′-N1 bond at the *Pf*OPRT and *Hs*OPRT transition states is further confirmed by the large [2′-^{3}H] and [1′-^{3}H] KIEs (discussion below). Since C1′-N1 distances greater than 2.6 Å cause no additional increase in [1, 3-$^{15}N_2$]KIEs, the C1′-N1 distances at these transition states are at least 2.6 Å (Figure 6).

[1′-^{14}C] and [1′-^{14}C, 1, 3-$^{15}N_2$] Primary KIEs

The primary [1′-^{14}C] KIE of OPRT is sensitive to motion along the reaction coordinate and also reflects the interactions of leaving group and nucleophile with the anomeric carbon. Thus, [1′-^{14}C] KIEs are often key parameters for determining mechanisms (S_N1 or S_N2) of *N*-ribosyltransferase enzymes.[58] A unity or slightly inverse [1′-^{14}C] KIE indicates a fully dissociative transition state (D_N*A_N) with an isolated ribooxacarbenium ion structure.[41] For transition states with weak to modest participation of leaving group or nucleophile, [1′-^{14}C] KIEs are in the range of 1.01 ~ 1.06.[41] The degree of participation for either leaving group or nucleophile influences the values of intrinsic [1, 3-$^{15}N_2$], [1′-^{3}H] and [2′-^{3}H] KIEs.[45,53,54]

The intrinsic [1′-^{14}C] KIEs of 1.034 for *Pf*OPRT and 1.035 for *Hs*OPRT are indicative of either early dissociative ($D_N^{‡}$*A_N) or late associative (D_N*$A_N^{‡}$) mechanisms (Figure 5 and Table 1).[45,53-55] Transition state candidates were optimized with systematically altered C1′-N1 and C1′-O^{PA} distances. Early dissociative ($D_N^{‡}$*A_N) structures were ruled out on the basis of unmatched [1, 3-$^{15}N_2$] KIEs (see the discussion above). Although several other structures exhibit similar calculated and intrinsic [1′-^{14}C] KIE values, only two structures could match [1′-^{14}C] KIEs as well as [1′-^{3}H] and [2′-^{3}H] KIEs (results below).

The C1′-$O^{phosphate}$ bond distances of 2.15 Å for the *Pf*OPRT and 2.14 Å for the *Hs*OPRT transition states gave the best agreement with the intrinsic KIEs (Figure 6). These distances were consistent with the [1′-^{14}C] KIEs of 1.034 and 1.035 and the large [1′-^{3}H] KIEs of 1.199 and 1.261. Formation of the ribooxacarbenium ion transition state accounts for the large [1′-^{3}H] KIE, while participation of the nucleophile gives rise to the significant [1′-^{14}C] KIEs resulting from the C1′-O^{PA} bond order.

To support the primary [1′-^{14}C] and [1, 3-$^{15}N_2$] KIE measurements the combined [1′-^{14}C, 1, 3-$^{15}N_2$] KIEs were measured. The intrinsic [1′-^{14}C, 1, 3-$^{15}N_2$] KIE of 1.068 for *Pf*OPRT is consistent with the product (1.063) of the [1′-^{14}C] KIE of 1.034 and [1, 3-$^{15}N_2$] KIE of 1.028. For *Hs*OPRT, the intrinsic [1′-^{14}C, 1, 3-$^{15}N_2$] KIE of 1.076 also agrees with the product of the

[1′-^{14}C] and [1, 3-$^{15}N_2$] KIEs within experimental errors (Table 1), supporting the accuracy of individual [1′-^{14}C] and [1, 3-$^{15}N_2$] KIEs used for transition state analysis.

[1′-^{3}H] α-secondary KIEs

The [1′-^{3}H] KIE originates primarily from the new out-of-plane mode as C1′ rehybridizes from sp^3 to sp^2 at the transition state. Small [1′-^{3}H] KIEs in *N*- ribosyltransferases suggest nucleophilic substitutions (S_N2) or partially dissociative $D_N^{\ddagger}*A_N$ transition states, while large [1′-^{3}H] KIEs are indicative of fully dissociative S_N1 or partially associative $D_N*A_N^{\ddagger}$ transition states. Increased out-of-plane bending mode of C1′-H1′ bond from sp^3 to sp^2 rehybridization at the transition state increases the magnitude of the [1′-^{3}H] KIE. However, a restricted stretching mode for the C1′-H1′ bond at the transition state decreases the [1′-^{3}H] KIEs. The out-of-plane bending mode is the more dominant effect.[59] The bending mode is sensitive to the variations of C1′-N1 bond distances and the participation of nucleophile. *Pf*OPRT and *Hs*OPRT show large intrinsic [1′-^{3}H] KIEs of 1.261 and 1.199, respectively (Figure 5). The magnitudes of the [1′-^{3}H] KIEs are consistent with full loss of the orotate dianion at the transition states, where the out-of-plane bending motions of ribooxacarbenium intermediate contribute strongly to the observed [1′-^{3}H] KIEs. Although calculated [1′-^{3}H] KIEs of 1.335 for *Pf*OPRT and 1.330 for *Hs*OPRT are substantially larger than the experimental KIEs (Table 1), it has been documented that [1′-^{3}H] KIEs are often overestimated by *in vacuo* computation due to condensed-phase uncertainty around the C1′-H1′ region.[46,53,60] Constraints from van der Waals interactions at the active sites are proposed to suppress the [1′-^{3}H] KIEs.

[2′-^{3}H] β-secondary KIEs

The [2′-^{3}H] KIE values are informative for ribosyl geometry, leaving group dissociation and nucleophilic participation at the transition states. They arise from hyperconjugation (orbital overlap) of the C2′- H2′ σ bond to the vacant $2p_z$ orbital of the anomeric carbon and the occupancy of the $2p_z$ orbital. Occupancy of $2p_z$ also depends on the extent of C1′-N1 dissociation and C1′-O^{PA} participation at the transition states. The intrinsic 2′-^{3}H KIEs of *Pf*OPRT and *Hs*OPRT of 1.116 and 1.129, respectively, are similar to the calculated [2′-^{3}H] KIEs of 1.142 for *Pf*OPRT and 1.140 for *Hs*OPRT (Table 1) for full dissociation of orotate, modest participation of the attacking nucleophile and 2′-C-*endo* ribosyl geometry (see below).

The large [2′-^{3}H] KIEs of *Pf*OPRT and *Hs*OPRT rule out early transition states with partial bonds to orotate ($D_N^{\ddagger}*A_N$). Computational modeling indicates small [2′-^{3}H] KIEs for early transition states with partially occupied $2p_z$ orbitals. The large [2′-^{3}H] KIEs of *Pf*OPRT and *Hs*OPRT also indicate ribosyl transition states with 2′-C-*endo* geometry and a H1′-C1′-C2′-H2′ dihedral angles of 71° for *Pf*OPRT and 70 ° for *Hs*OPRT (Figure 6). In contrast, 2′-C-*exo* transition states give smaller [2′-^{3}H] KIEs, where the H1′-C1′-C2′-H2′ dihedral angle of 2′-C-*exo* conformers is close to zero and thus compromises C2′-H2′→C1′-$2p_z$ hyperconjugation.

[5′-$^3H_2$] Remote KIEs

The intrinsic [5′-$^3H_2$] KIEs are 1.013 for *Pf*OPRT and 1.019 for *Hs*OPRT (Table 1) even through 5′-$^3H_2$ are four bonds distant from C1′ and not expected be influenced by chemistry at the reaction center. These modest [5′-$^3H_2$] KIEs reflect remote conformational changes at the 5′- regions in transition state formation and arise from the product of the 5′-H-*proR* and 5′-H-*proS* KIEs. Computational studies on the 5′-conformation were accomplished by constraints selected from the OPRT crystal structures containing OMP molecules.[56,57] Optimized structures with a restricted O4′-C4′-C5′-5′-H-*proR* dihedral angle of −137° gave consistent [5′-$^3H_2$] KIE values for *Pf*OPRT and *Hs*OPRT (Table 1). Remote KIEs at the 5′-regions indicates bond distortion remote from chemistry imposed by the enzyme catalytic sites.

[4′-^{3}H] Remote KIEs

The intrinsic [4′-^{3}H] KIEs are 0.974 for *Pf*OPRT and 0.962 for *Hs*OPRT (Figure 5). The [4′-^{3}H] KIE is influenced by hyperconjugation between the C4′-H4′ σ^* antibonding orbital and the O4′ long pair.[53] An oxacarbenium ion transition state causes the O4′ n_p electrons to redistribute toward the positively-charged anomeric carbon, causing decreased hyperconjugation between the C4′-H4′ σ^* antibonding orbital and the O4′ n_p electrons. A shorter C4′-H4′ bond at the transition state relative to the substrate causes inverse [4′-^{3}H] KIEs (Table 3). The [4′-^{3}H] KIE is also influenced by polarization of the 3′-hydroxyl group, which causes normal [4′-^{3}H] KIEs.[54,55] The [4′-^{3}H] KIEs of the solved *Pf*OPRT and *Hs*OPRT transition states were calculated to be 0.972, which agree with the intrinsic [4′-^{3}H] KIEs of 0.962 and 0.974. The small inverse [4′-^{3}H] KIEs of *Pf*OPRT and *Hs*OPRT are consistent with a well-developed ribocation transition state. The inverse [4′-^{3}H] KIEs indicate that the 3′-hydroxyl groups are not polarized in *Pf*OPRT and *Hs*OPRT transition states, as they are in some *N*-ribosyltransferases.[53,55]

Kinetic Constants

With OMP and PA as a slow substrate analogue for PPi, the catalytic efficiency (k_{cat}/K_m) for *Pf*OPRT and *Hs*OPRT were approximately equivalent at 4.8×10^3 and 7.9×10^3 M^{-1} s^{-1}, respectively. These values are reduced 110-fold for *Pf*OPRT and 8.3-fold for *Hs*OPRT relative to their (k_{cat}/K_m) values with PPi as the nucleophile (Table 4). These catalytic reductions are sufficient to give near-intrinsic KIE values as described above. The differences are dominated by k_{cat} changes, and as the K_m values are all in the range of 1 to 4 μM, relatively tight binding as expected for intermediates in a linear, essential biosynthetic pathway.

Leaving Group Activation

*Pf*OPRT and *Hs*OPRT can achieve their oxacarbenium ion transition states through leaving group activation, oxacarbenium ion formation or 2′-hydroxyl ionization (Figure 7). *p*-Nitrophenyl β-D-ribose 5′-phosphate was used to distinguish leaving group activation from mechanisms of ribooxacarbenium ion formation and/or stabilization. If the enzyme activates the substrate through ribosyl activation, the *p*-nitrophenyl group provides an excellent leaving group, needing no enzymatic assistance, and *p*-nitrophenyl β-D-ribose 5′-phosphate would be an excellent substrate.[35] Assays indicated that *Pf*OPRT did not catalyze the O-glycosidic bond cleavage of *p*-nitrophenyl β-D-ribose 5′-phosphate under conditions that could detect 10^{-6} of normal activity. Poor catalytic activity of *Pf*OPRT and *Hs*OPRT for the *p*-nitrophenyl β-D-ribose 5′-phosphate establishes that leaving group activation is a major force in OPRT reactions, therefore, base recognition plays an important catalytic role. The intrinsic KIEs for *Pf*OPRT and *Hs*OPRT indicated that orotate leaving group is not activated through protonation of any single group. However, leaving group activation may be accomplished through multiple hydrogen bond and/or ionic interactions with active site residues. Crystal structures of the yeast OPRT in complex with orotate, PRPP and Mg^{2+} ion support this proposal with orotate O4 in H-bond distance with a peptide bond NH and a guanidinium ion, N3 in contact with a peptide bond oxygen and the carboxylate hydrogen bonded to a threonine sidechain, a peptide NH and two ordered water molecules. Likewise, O2 of orotate also contacts two ordered water molecules.[57] Similar interaction networks are also observed in the crystal structures of *St*OPRT in complex with orotate, PRPP and Mg^{2+}.[56] In the physiological direction, it is necessary to form dianionic orotate (from the monoanion) to form the proposed transition state. In *St*OPRT, a conserved water molecule is within H-bond distance to N1H of orotate and also interacts with oxygens of the orotate carboxyl and the pyrophosphate. The water can be proposed to act as proton transfer bridge to deprotonate N1 to make the dianionic transition state species of orotate.

Nitrophenyl Ribosides as Inhibitors of OPRTs

Lack of catalytic activity with substrate analogues can also indicate poor binding, but this is not the case for nitrophenyl ribosides with the OPRTs. Inhibition assays indicated that *p*-nitrophenyl β-D-ribose 5′-phosphate is a competitive inhibitor against OMP for both *Pf*OPRT and *Hs*OPRT with K_i values of 40 and 41 nM, respectively (Table 4). Thus, *p*-nitrophenyl β-D-ribose 5′-phosphate binds substantially better than OMP to give K_m/K_i values of 93 and 38 for *Pf*OPRT and *Hs*OPRT, respectively. The role of the phosphate monoester in inhibitor binding was evaluated with *p*-nitrophenyl β-D-ribose which also inhibited both *Pf*OPRT and *Hs*OPRT to give K_i values of 188 and 121 nM, respectively (Table 4). Orotidine was found to be a poor OPRT substrate with a K_m of 96 μM for *Pf*OPRT and 91 μM for *Hs*OPRT with weak k_{cat} values of 0.042 s^{-1} for *Pf*OPRT and 0.024 s^{-1} for *Hs*OPRT. It is uncommon for nucleotide-binding enzymes to show high affinity or substrate activity without the 5′-phosphate, and the relatively tight binding of *p*-nitrophenyl β-D-ribose to both *Pf*OPRT and *Hs*OPRT is a promising lead for the design of cell-permeable analogues that retain strong binding to parasite and/or human OPRTs.

Comparison of Transition State Structures

The transition state of *St*OPRT has been reported to be $D_N^{\ddagger}*A_N$, different from the late associative features ($D_N*A_N^{\ddagger}$) of *Pf*OPRT and *Hs*OPRT transition states.[37] The transition state of *St*OPRT has a partially broken C1′-N1 bond with the distance of 1.85 Å and the nucleophile, O^{PA}, is >3.0 Å away from the anomeric carbon. Therefore, the *St*OPRT transition state is reached prior to full formation of the oxacarbenium ion. In contrast, *Pf*OPRT and *Hs*OPRT transition states show late associative characteristics ($D_N*A_N^{\ddagger}$) with full dissociation of orotate and partial participation of the O^{PA} nucleophile. These OPRT transition states can be distinguished by distinct C1′-N1 and C1′-O^{PA} bond orders. The primary [1′-^{14}C] KIE of 1.03 and α-secondary [1′-^{3}H] KIE of 1.17 have also been reported for yeast OPRT, similar to those of *Pf*OPRT and *Hs*OPRT and suggest a similar dissociative transition state.[61]

*Pf*OPRT and *Hs*OPRT are *N*-ribosyltransferases with late associative $D_N*A_N\ddagger$ transition states, similar to that of human 5'-methylthioadenosine phosphorylase (MTAP).[55] Another group of N-ribosyltransferases, namely those of *S. pneumoniae* 5'-methylthioadenosine nucleosidase (*Sp*MTAN), *E.coli* MTAN (*Ec*MTAN), human purine nucleoside phosphorylase (*Hs*PNP) and *Pf*PNP exhibit fully dissociative S_N1 transition states with fully developed ribocations. A third group, including *N. meningitides* MTAN (*Nm*MTAN) and bovine PNP (*Bt*PNP) have early S_N1, partially dissociative $D_N\ddagger*A_N$ transition states with significant bond order between anomeric carbon and leaving group.[41,46,53,54,62] These diverse transition state structures among *N*-ribosyltransferase enzymes can be exploited to develop target-specific transition state analogue inhibitors.

Conclusion

The transition state structures of *Pf*OPRT and *Hs*OPRT were determined using density functional calculations constrained by experimental intrinsic KIEs. They have similar transition state structures despite low sequence identity. *Pf*OPRT and *Hs*OPRT transition transition states with fully state structures are characterized by late dissociative $D_N*A_N\ddagger$ dissociated orotate, ribooxacarbenium ion character, partially formed nucleophilic bonds and 2′-C-*endo* ribosyl geometry. The lack of catalytic activity with *p*-nitrophenyl β-D-ribose 5′-phosphate establishes leaving group activation as major force in the reactions catalyzed by *Pf*OPRT and *Hs*OPRT. Despite its poor substrate activity, *p*-nitrophenyl β-D-ribose 5′-phosphate binds much tighter than the OMP substrate and retains most of the binding energy in the absence of the 5′-phosphate. The *Pf*OPRT and *Hs*OPRT transition states are distinct from that of *St*OPRT, which featured an early dissociative transition state with no nucleophilic

participation. Among the known transition state structures of *N*-ribosyltransferases, the transition states of *Pf*OPRT and *Hs*OPRT are similar only to that of human MTAP and are distinct from those of *St*OPRT, *Sp*MTAN, *Ec*MTAN, *Nm*MTAN, *Hs*PNP, *Pf*PNP and *Bt*PNP. The transition state structures of *Pf*OPRT and *Hs*OPRT provide information for the design of transition state analogue inhibitors against the OPRT isozymes.

Supplementary Material

Refer to Web version on PubMed Central for supplementary material.

Acknowledgement

We thank Drs. Richard H. Furneaux and Peter C. Tyler (Industrial Research Ltd., New Zealand) for the synthesis of *p*-nitrophenyl β-D-ribose and Dr. Maria B. Cassera (Department of Biochemistry, Albert Einstein College of Medicine) for providing the Ag-dNK. We also thank Prof. Jiali Gao in University of Minnesota Supercomputer Institute for allocation of computer time. This work was supported by NIH grant AI049512.

References

1. Guerin PJ, Olliaro P, Nosten F, Druilhe P, Laxminarayan R, Binka F, Kilama WL, Ford N, White NJ. Lancet. Infect. Dis 2002;2:564–573. [PubMed: 12206972]
2. White NJ. J. Clin. Invest 2004;113:1084–1092. [PubMed: 15085184]
3. ter Kuile FO, van Eijk AM, Filler SJ. JAMA 2007;297:2603–2616. [PubMed: 17579229]
4. Jones ME. Annu. Rev. Biochem 1980;49:253–279. [PubMed: 6105839]
5. Baldwin J, Michnoff CH, Malmquist NA, White J, Roth MG, Rathod PK, Phillips MA. J. Biol. Chem 2005;280:21847–21853. [PubMed: 15795226]
6. Krungkrai SR, DelFraino BJ, Smiley JA, Prapunwattana P, Mitamura T, Horii T, Krungkrai J. Biochemistry 2005;44:1643–1652. [PubMed: 15683248]
7. Krungkrai SR, Aoki S, Palacpac NM, Sato D, Mitamura T, Krungkrai J, Horii T. Mol. Biochem. Parasitol 2004;134:245–255. [PubMed: 15003844]
8. Krungkrai J. Biochim. Biophys. Acta 1995;1243:351–360. [PubMed: 7727509]
9. Seymour KK, Lyons SD, Phillips L, Rieckmann KH, Christopherson RI. Biochemistry 1994;33:5268–5274. [PubMed: 7909690]
10. Krungkrai J, Krungkrai SR, Phakanont K. Biochem. Pharmacol 1992;43:1295–1301. [PubMed: 1348618]
11. Gero AM, O'Sullivan WJ. Blood Cells 1990;16:467–484. [PubMed: 2257323]
12. Schramm VL, Grubmeyer C. Prog. Nucleic Acid Res. Mol. Biol 2004;78:261–304. [PubMed: 15210333]
13. Henriksen A, Aghajari N, Jensen KF, Gajhede M. Biochemistry 1996;35:3803–3809. [PubMed: 8620002]
14. Scapin G, Ozturk DH, Grubmeyer C, Sacchettini JC. Biochemistry 1995;34:10744–10754. [PubMed: 7545004]
15. Grubmeyer C, Segura E, Dorfman R. J. Biol. Chem 1993;268:20299–202304. [PubMed: 8376388]
16. Suchi M, Mizuno H, Kawai Y, Tsuboi T, Sumi S, Okajima K, Hodgson ME, Ogawa H, Wada Y. Am. J. Hum. Genet 1997;60:525–539. [PubMed: 9042911]
17. Yablonski MJ, Pasek DA, Han BD, Jones ME, Traut TW. J. Biol. Chem 1996;271:10704–10708. [PubMed: 8631878]
18. Traut TW, Jones ME. Prog. Nucleic Acid Res. Mol. Biol 1996;53:1–78. [PubMed: 8650301]
19. Jacquet M, Guilbaud R, Garreau H. Mol. Gen. Genet 1988;211:441–445. [PubMed: 2835631]
20. Wittmann JG, Heinrich D, Gasow K, Frey A, Diederichsen U, Rudolph MG. Structure 2008;16:82–92. [PubMed: 18184586]
21. Quemeneur L, Beloeil L, Michallet MC, Angelov G, Tomkowiak M, Revillard JP, Marvel J. J. Immunol 2004;173:4945–4952. [PubMed: 15470036]

22. Chu E, Callender MA, Farrell MP, Schmitz JC. Cancer Chemother. Pharmacol 2003;52(Suppl 1):80–89.
23. Christopherson RI, Lyons SD, Wilson PK. Acc. Chem. Res 2002;35:961–971. [PubMed: 12437321]
24. Allison AC. Immunopharmacology 2000;47:63–83. [PubMed: 10878284]
25. Herrmann ML, Schleyerbach R, Kirschbaum BJ. Immunopharmacology 2000;47:273–289. [PubMed: 10878294]
26. Weber G. Biochemistry (Mosc) 2001;66:1164–73. [PubMed: 11736638]
27. Wolfenden R, Snider MJ. Acc. Chem. Res 2001;34:938–945. [PubMed: 11747411]
28. Schramm VL. J. Biol. Chem 2007;282:28297–28300. [PubMed: 17690091]
29. Schramm VL. Curr. Opin. Struct. Biol 2005;15:604–613. [PubMed: 16274984]
30. Schramm VL. Arch. Biochem. Biophys 2005;433:13–26. [PubMed: 15581562]
31. Schramm VL. Nucleic Acids Res. Suppl 2003:107–108. [PubMed: 14510403]
32. Schramm VL. Meth. Enzymol 1999;308:301–355. [PubMed: 10507010]
33. Schramm VL. Acc. Chem. Res 2003;36:588–596. [PubMed: 12924955]
34. Cleland WW. Arch. Biochem. Biophys 2005;433:2–12. [PubMed: 15581561]
35. Mazzella LJ, Parkin DW, Tyler PC, Furneaux RH, Schramm VL. J. Am. Chem. Soc 1996;118:2111–2112.
36. Knecht W, Petersen GE, Sandrini MP, Sondergaard L, Munch-Petersen B, Piskur J. Nucleic Acids Res 2003;31:1665–72. [PubMed: 12626708]
37. Tao W, Grubmeyer C, Blanchard JS. Biochemistry 1996;35:14–21. [PubMed: 8555167]
38. Rising KA, Schramm VL. J. Am. Chem. Soc 1994;116:6531–6536.
39. Luo M, Schramm VL. J. Am. Chem. Soc. 2008
40. Luo M, Singh V, Taylor EA, Schramm VL. J. Am. Chem. Soc 2007;129:8008–8017. [PubMed: 17536804]
41. Singh V, Lee JE, Nunez S, Howell PL, Schramm VL. Biochemistry 2005;44:11647–11659. [PubMed: 16128565]
42. Parkin DW, Leung HB, Schramm VL. J. Biol. Chem 1984;259:9411–9417. [PubMed: 6746654]
43. Fox SW, Johnson JE. Science 1956;124:923–5. [PubMed: 13380403]
44. Takeyama S, Noguchi T, Miura Y, Ishidate M. Pharm. Bull 1956;4:492–494. [PubMed: 13408094]
45. Luo M, Li L, Schramm VL. Biochemistry 2008;47:2565–76. [PubMed: 18281957]
46. Lewandowicz A, Schramm VL. Biochemistry 2004;43:1458–1468. [PubMed: 14769022]
47. Rose IA. Meth. Enzymol 1980;64:47–59. [PubMed: 7374457]
48. Frisch, MJ., et al. Gaussian, Inc.; Pittsburgh PA: 2002.
49. Anisimov V, Paneth P. J. Math. Chem 1999;26:75–86.
50. Flükiger, P.; Lüthi, HP.; Portmann, S.; Weber, J. Swiss Center for Scientific Computing, M.; Switzerland: 20002002.
51. Portmann S, Lüthi HP. CHIMIA 2000;54:766–770.
52. Northrop DB. Biochemistry 1975;14:2644–2651. [PubMed: 1148173]
53. Singh V, Schramm VL. J. Am. Chem. Soc 2007;129:2783–2795. [PubMed: 17298059]
54. Singh V, Luo M, Brown RL, Norris GE, Schramm VL. J. Am. Chem. Soc 2007;129:13831–13833. [PubMed: 17956098]
55. Singh V, Schramm VL. J. Am. Chem. Soc 2006;128:14691–14696. [PubMed: 17090056]
56. Scapin G, Grubmeyer C, Sacchettini JC. Biochemistry 1994;33:1287–1294. [PubMed: 8312245]
57. Gonzalez-Segura L, Witte JF, McClard RW, Hurley TD. Biochemistry 2007;46:14075–14086. [PubMed: 18020427]
58. Berti PJ, Tanaka KSE. Adv. Phys. Org. Chem 2002;37:239–314.
59. Pham TV, Fang YR, Westaway KC. J. Am. Chem. Soc 1997;119:3670–3676.
60. McCann JA, Berti PJ. J. Am. Chem. Soc 2007;129:7055–7064. [PubMed: 17497857]
61. Goitein RK, Chelsky D, Parsons SM. J. Biol. Chem 1978;253:2963–2971. [PubMed: 641051]
62. Kline PC, Schramm VL. Biochemistry 1993;32:13212–13219. [PubMed: 8241176]

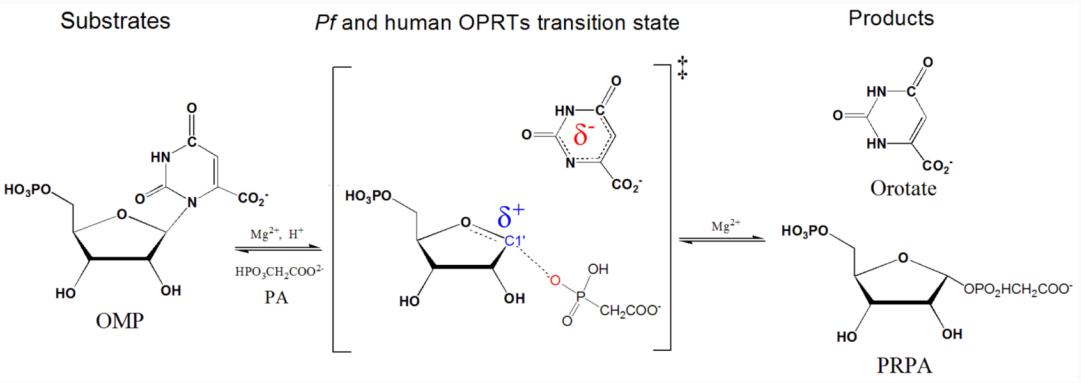

Figure 1.
Reaction catalyzed by *Pf*OPRT and *Hs*OPRT with phosphonoacetic acid (PA) as substrate.

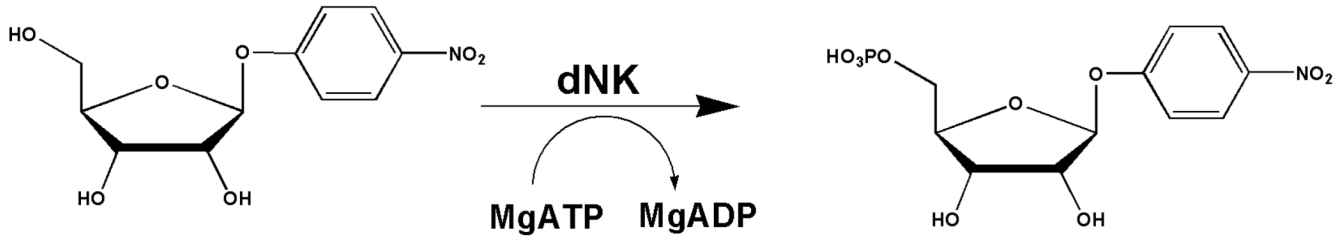

Figure 2.
Synthesis of *p*-nitrophenyl β-D-ribose 5′-phosphate.

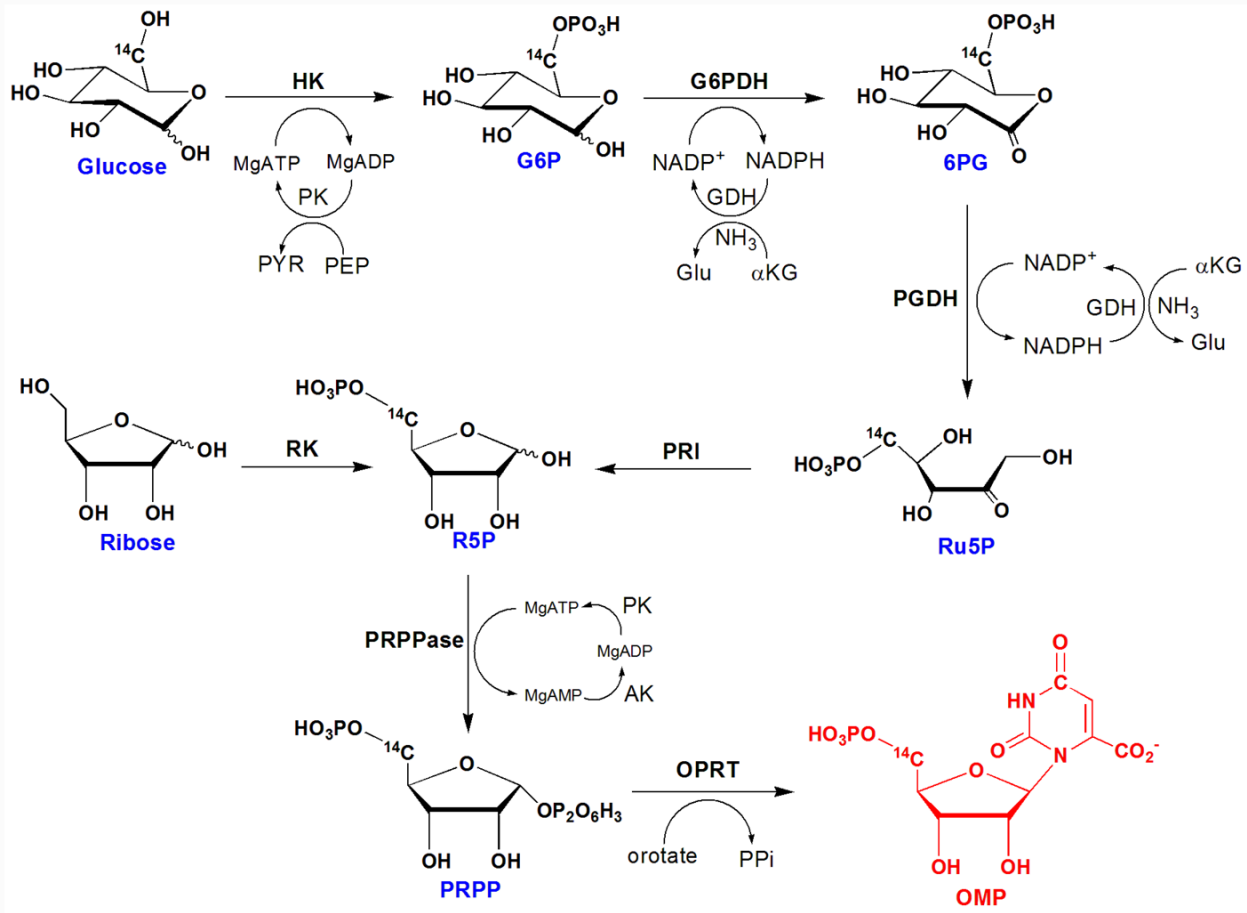

Figure 3.

Synthesis of isotopically labeled OMPs using [5′-^{14}C]OMP as an example. [1′-^{14}C]-, [1′-^{3}H]-, [2′-^{3}H]-, [4′-^{3}H]-, [5′-^{14}C]-, [5′-$^{3}H_2$]-, [1, 3-$^{15}N_2$, 5′-^{14}C]-, [3-^{15}N, 5′-^{14}C]- and [1, 3-$^{15}N_2$, 1′-^{14}C]OMP were prepared from isotopically labeled riboses, glucoses and orotates through one-pot, stepwise enzymatic reactions. The enzyme mixtures used for the synthesis contain ribokinase (RK), hexokinase (HK), glucose-6-phosphate dehydrogenase (G6PDH), phosphogluconic acid dehydrogenase (PGDH), L-glutamic dehydrogenase (GDH), phosphoriboisomerase (PRI), adenylate kinase (AK), pyruvate kinase (PK), phospho-D-ribosyl-1-pyrophosphate synthase (PRPPase) and orotate phosphoribosyltransferase (OPRT).

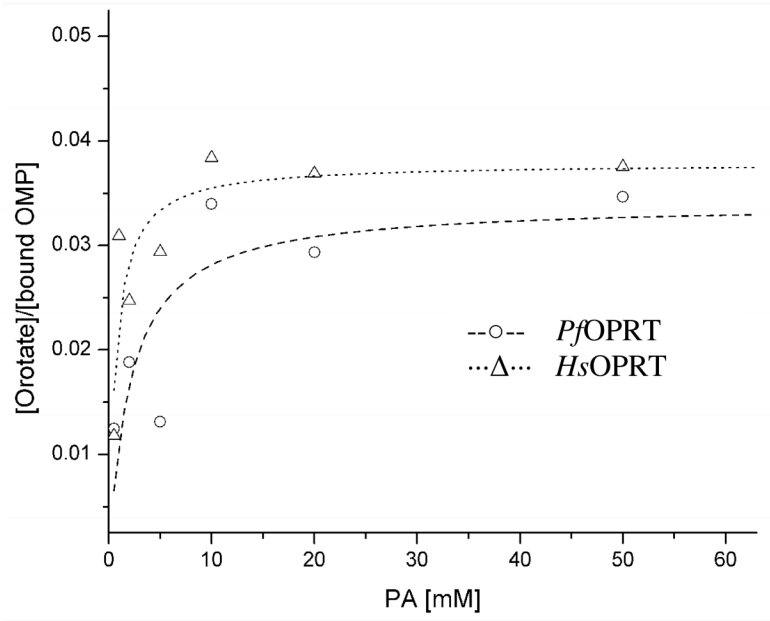

Figure 4.

Forward commitments to catalysis by *Pf*OPRT and *Hs*OPRT. Isotope trapping experiments were performed to measure the forward commitment factors. [1, 3-$^{15}N_2$; 5′-^{14}C]OMP was pre-incubated with OPRTs for 10 s and then rapidly mixed with chase buffers including cold OMP and various concentrations of PA. After five catalytic turnovers, the generated products were isolated by charcoal column chromatography and analyzed on the basis of the total radioactivity. The fractions of product formed vs bound substrate at time zero were plotted against PA concentrations. Forward commitment factors were calculated on the basis of $C_f = \frac{Y_{max}}{1 - Y_{max}}$ to give the C_f of *Pf*OPRT (--○--) of 0.035 ± 0.006 and C_f of *Hs*OPRT (···Δ···) of 0.042 ± 0.003 (see method for details).

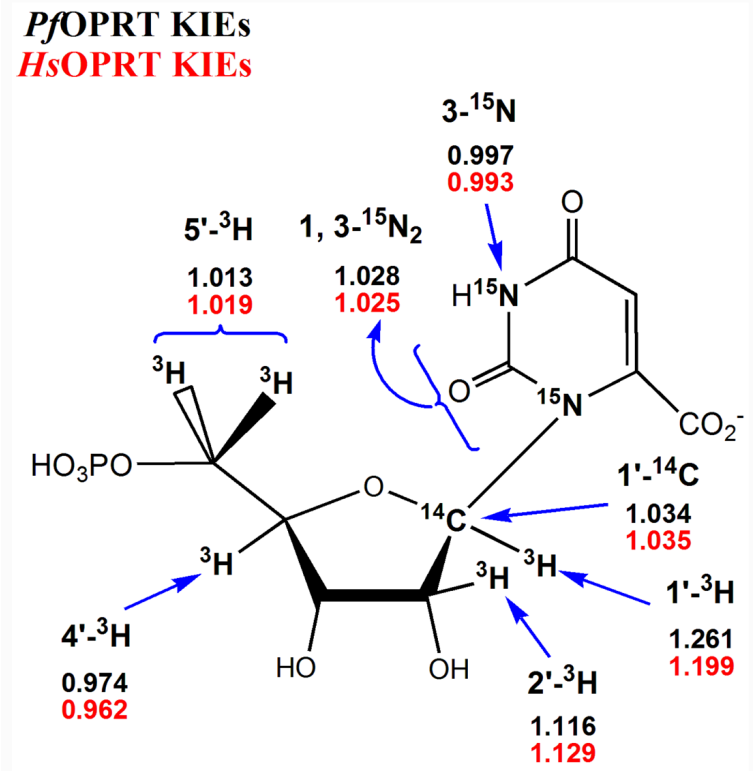

Figure 5.
Intrinsic KIEs for *Pf*OPRT and *Hs*OPRT. The positions for isotopic labeling are indicated in the substrate OMP.

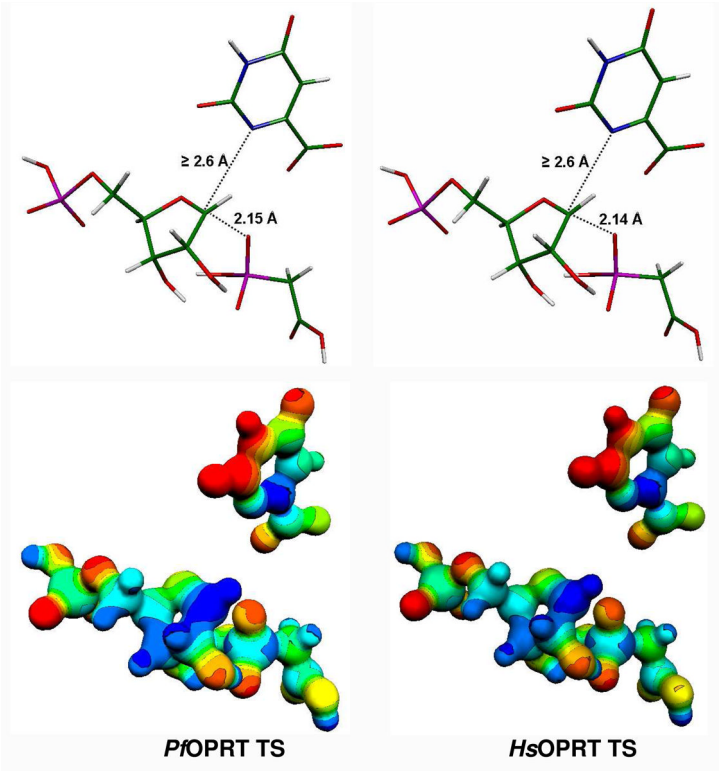

Figure 6.

Transition state structures of *Pf*OPRT and *Hs*OPRT (Stick and MEP modes). The transition state structures were determined *in vacuo* by hybrid density functional theory implemented in Gaussian 98 using B3LYP functional and the 6-31G (d, p) basis sets. The distances in the reaction coordinate (C1′-N1 and C1′-O^{PA}) for *Pf*OPRT and *Hs*OPRT transition states are shown. The molecular electrostatic potential (MEP) surfaces were generated by the CUBE subprogram of Gaussian 98 and are visualized using Molekel 4.0 at a density of 0.2 electron/$Å^3$. Blue is electron deficient (cationic) and red is electron rich (anionic) in this rendering and in Figure 7.

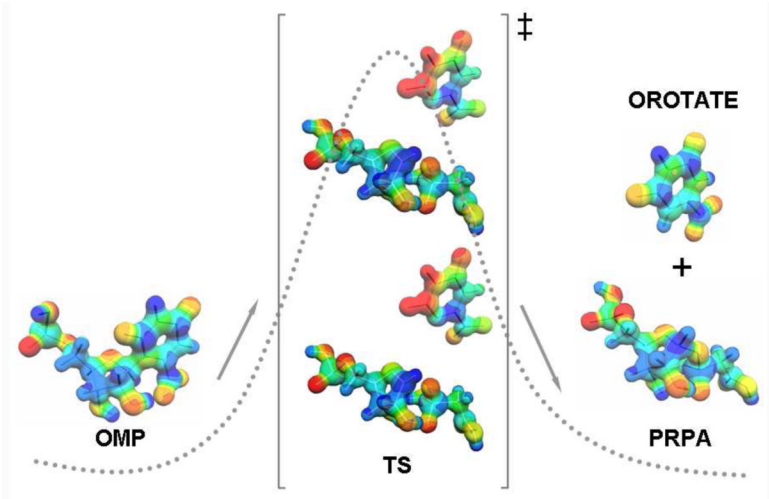

Figure 7.

Reaction coordinate for the conversion from OMP to the products orotate and 5-phosphoribosyl 1-phophonoacetic acid (PRPA). The transition state structures of *Pf*OPRT and *Hs*OPRT are shown. MEP surfaces were generated by the CUBE subprogram of Gaussian 98 and visualized using Molekel 4.0 at a density of 0.2 electron/Å^3.

Table 1

Intrinsic KIEs[a] of *Pf*OPRT and *Hs*OPRT and computationally matched KIEs[b].

Isotopically labeled OMP	KIEs type	*Pf*OPRT KIEs		*Hs*OPRT KIEs	
		Intrinsic	Calcd.	Intrinsic	Calcd.
[1′-^{3}H] + [5′-^{14}C]	α-secondary	1.261 ± 0.014	1.335	1.199 ± 0.015	1.330
[1′-^{14}C] + [4′-^{3}H]	primary	1.034 ± 0.002	1.034	1.035 ± 0.003	1.035
[2′-^{3}H] + [5′-^{14}C]	β-secondary	1.116 ± 0.006	1.142	1.129 ± 0.009	1.140
[1, 3-$^{15}N_2$, 5′-^{14}C] + [4′-^{3}H]	primary	1.028 ± 0.003	1.025	1.025 ± 0.005	1.025
[3-^{15}N, 5′ ^{14}C] + [4′-^{3}H]	β-secondary	0.997 ± 0.003	1.004	0.993 ± 0.002	1.004
[1, 3-$^{15}N_2$, 1′-^{14}C] + [4′-^{3}H]	primary	1.068 ± 0.003	1.060	1.076 ± 0.005	1.061
[4′-^{3}H] + [5′-^{14}C]	γ-secondary	0.974 ± 0.003	0.972	0.962 ± 0.002	0.972
[5′-$^{3}H_2$] + [5′-^{14}C]	δ-secondary	1.013 ± 0.012	1.019	1.019 ± 0.002	1.018

[a] Intrinsic KIEs were obtained by correcting for remote label KIEs and for forward commitment factors. Experimental KIEs $^{X}(V/K)$ and intrinsic KIEs ^{X}k are within experimental errors due to the small commitment factors. Each KIE was measured with at least 5 replicates.

[b] Computationally matched KIEs were established from the Gaussian 98 transition state structures optimized to the family of intrinsic isotope effects. The calculated KIEs compare the bond frequencies from substrate and optimized transition states using the ISOEFF98 program.

Table 2

Effect of orotate protonation and/or tautomerization on N1 and N3 KIEs.

	Intrinsic or Calculated KIEs		
	N1	**N3**	**N1 & N3**
*Hs*OPRT	1.032 ± 0.007	0.993 ± 0.002	1.025 ± 0.005
*Pf*OPRT	1.031 ± 0.006	0.997 ± 0.003	1.028 ± 0.003
Orotate[a]	1.021	1.004	1.025
O2 protonation[b]	1.014	0.999	1.013
O4 protonation[b]	1.019	1.001	1.020
O7 protonation[b]	1.019	1.003	1.022
O-2H tautomer[a]	1.018	1.014	1.032
O-4H tautomer[a]	1.022	1.014	1.037
O-2H tautomer & O7 protonation[b]	1.017	1.013	1.030
O-4H tautomer & O7 protonation[b]	1.022	1.013	1.035
O-2H tautomer & O4 protonation[b]	1.016	1.008	1.023
O-2H tautomer & O4 protonation & O7 protonation[c]	1.014	1.006	1.020

[a] Dianionic.

[b] Monoanionic.

[c] Neutral.

Table 3

Key geometric changes from the reactants (OMP and PA)(GS) to the transition states (TS) of *Pf*OPRT and *Hs*OPRT.

		***Pf*OPRT**	***Hs*OPRT**
bond type	**bond length (Å) (GS)**	**bond length (Å) (TS)**	**bond length (Å) (TS)**
C1′-N1	1.481	≥ 2.600	≥ 2.600
C1′-O^{PA}	> 3.0	2.150	2.140
C1′-O4′	1.407	1.278	1.279
C1′-C2′	1.538	1.517	1.518
C1′-H1′	1.092	1.082	1.082
C2′-H2′	1.095	1.107	1.107
C4′-H4′	1.096	1.091	1.091
C4′-O4′	1.456	1.530	1.530
N1-C2	1.401	1.358	1.358
N1-C6	1.393	1.355	1.355
C2-O2	1.221	1.252	1.252
C2-N3	1.389	1.416	1.416
N3-H3	1.011	1.011	1.011
C4-O4	1.232	1.257	1.257

Table 4

Kinetic parameters for *Pf*OPRT and *Hs*OPRT with OMP and *p*-nitrophenyl β-D-ribose 5′-phosphate [a].

		OMP			*p*-Nitrophenyl β-D-ribose 5′-phosphate	*p*-Nitrophenyl β-D-ribose
enzyme	**substrate**	***k*cat (s^{-1})**	**K_m (μM)**	***k*cat/*K*m (M^{-1} s^{-1})**	**K_i[b] (nM)**	
*Pf*OPRT	PA	0.014 ± 0.002	2.90 ± 1.09	4.8×10^3	---	---
	PP_i	1.96 ± 0.29	3.73 ± 1.36	5.3×10^5	40 ± 21	188 ± 40
*Hs*OPRT	PA	0.017 ± 0.002	2.14 ± 0.61	7.9×10^3	---	---
	PP_i	0.10 ± 0.01	1.55 ± 0.61	6.5×10^4	41 ± 19	121 ± 30

[a] Assays were performed at 25 °C by adding purified *Pf*OPRT or *Hs*OPRT into mixtures containing 50 mM Tris-HCl (pH = 8.0), 5 mM $MgCl_2$, 20 mM PA or 1 mM PP_i and varied concentrations of *p*-nitrophenyl β-D-ribose 5′-phosphate, *p*-nitrophenyl β-D-ribose, OMP and PA or PPi.

[b] The K_i value is for the inhibitors with respect to competitive inhibition for OMP.